Constant Power Output Wireless Charging System for Automatic Guided Vehicle Using the Primary Side Controllable Magnetic Flux Capacitor

Zhenjie Li, *Member, IEEE*, Qihao Dong, Yuhong Bai, Dechun Yuan, and Yiqi Liu, *Member, IEEE*

***Abstract*—This article proposes a novel primary side controllable magnetic flux capacitor (CMFC) for a wireless charging system (WCS) in automatic guided vehicles (AGVs). It aims to address two challenges: zero-voltage switching (ZVS) for the full-bridge inverter and constant power (CP) charging for the battery, which are affected by variations in the transmitter coil's self-inductance and the magnetic coupler's mutual inductance, as well as the battery's equivalent load resistance. The CMFC also replaces the resonant capacitor on the primary side. First, the circuit structure of the designed WCS for AGVs and the two problems existing in it are analyzed. Therefore, the CMFC is proposed to address the drawbacks of similar existing methods in resolving these problems. Second, from the hardware aspects, the concept of "controllable magnetic flux principle" and parameter design method for the CMFC is given. From the software aspects, the closed-loop control strategy for the WCS with CMFC is given. Finally, an engineering prototype is constructed. It verifies that the designed WCS can achieve 350-W CP charging and 92.7% efficiency with equivalent load resistance from 2.57 to 8.33 Ω and misalignment up to 40% or 10% of the transmitter coil's width in *x*- or *y*-direction.**

***Index Terms*—Automatic guided vehicle AGV), constant power (CP) charging with the zero-voltage switching (ZVS), controllable magnetic flux capacitor (CMFC), primary side control method, wireless power transfer.**

I. Introduction

NOWADAYS, automatic guided vehicles (AGVs) have been extensively utilized in logistics and manufacturing due to their flexible routing, advancing the unmanned industry. However, their automation potential is still highly constrained by limited battery capacity and cumbersome plug-in/plug-out operations. To address these issues, wireless charging systems (WCS) emerge as a very promising solution, offering enhanced safety and automation by utterly eliminating direct electrical connections. Despite these benefits, further improvements are still essential to ensure the highly efficient operation of the WCS for AGVs, particularly in the following areas.

1) Considering that AGVs may not stop precisely at the charging position, misalignment of the magnetic coupler affects the mutual inductance. Moreover, the small air gap between the AGV chassis and the ground typically limits the transmission distance of the magnetic coupler. Under this condition, when the misalignment occurs, the uneven magnetic field may significantly influence the transmitter coil's self-inductance, which further disrupts zero-voltage switching (ZVS) in the full-bridge inverter [3], [4].
2) The WCS's charging performance is typically affected by two main factors: the varying equivalent load resistance of the battery during dynamic charging and the changes in the transmitter coil's self-inductance and the magnetic coupler's mutual inductance. Hence, it is necessary to use a closed-loop controlled power adjustment circuit to solve this problem. Traditional battery charging methods [5]. [6], such as the constant current (CC) followed by the constant voltage (CV) charging, have the following limitations: the maximum charging power is only achieved near the end of CC charging, leading to underutilization of the WCS's maximum power capability and a slow charging rate. Although increasing the charging current can address this, it requires excessive thermal design. As shown in Fig. 1, to overcome the above problems, constant power (CP) charging is proposed [7], [8]. By decreasing the charging current as the battery voltage increases, CP charging fully utilizes the WCS's maximum power capability, resulting in faster charging speeds and reduced thermal issues.

Furthermore, the analysis of the above two problems and the proposal of an efficient solution are motivations of this article; then, a WCS for AGVs is further designed to verify it.

A. Relevant Research Works

The misalignment problem can be solved by designing and optimizing the magnetic coupler and compensation topology, as well as the system-level closed-loop control. First, double-D

Received 4 May 2025; revised 20 July 2025 and 8 September 2025; accepted 19 September 2025. Date of publication 24 September 2025; date of current version 23 December 2025. This work was supported in part by the Fundamental Research Funds for the Central Universities under Grant 2572023CT15, in part by the China Postdoctoral Science Foundation under Grant 2022M710641, and in part by the National Natural Science Foundation of China under Grant 52107001. Recommended for publication by Associate Editor M. Ponce-Silva. *(Corresponding author: Dechun Yuan.)*

Zhenjie Li, Qihao Dong, Dechun Yuan, and Yiqi Liu are with the College of Computer and Control Engineering, Northeast Forestry University, Harbin 150040, China (e-mail: lizhenjie0725@nefu.edu.cn; lnjzdqh@nefu.edu.cn; 15114558998@nefu.edu.cn; nefukzch@nefu.edu.cn).

Yuhong Bai is with the College of Mechanical and Electrical Engineering, Northeast Forestry University, Harbin 150040, China (e-mail: 2022111829@nefu.edu.cn).

Color versions of one or more figures in this article are available at https://doi.org/10.1109/TPEL.2025.3613983.

Digital Object Identifier 10.1109/TPEL.2025.3613983

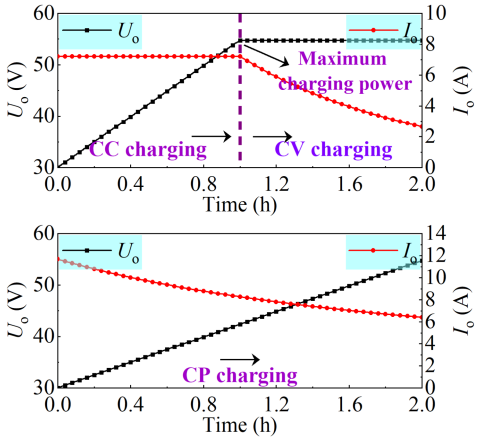

Fig. 1. Comparison between CC/CV and CP charging.

(DD) pads and bipolar pads are designed to generate a uniform magnetic field, thereby minimizing the mutual inductance's variation when misalignment occurs [9], [10]. Besides, hybrid coil structures, such as the combined solenoid and DD coils, quadruple-D and square coil overlays, and reverse-series third coils, demonstrate strong antimisalignment ability [11], [12], [13]. These magnetic couplers may suffer from problems, such as a limited misalignment tolerance range and intricate parameter optimization. Second, high-order compensation topology, such as the S/SP and PS/P, can improve the misalignment tolerance [12], [14]. The hybrid compensation topologies that combine two topologies whose output gain is opposite to the mutual inductance change achieve the CP within a suitable misalignment range [15], [16]. Detuned compensation topology, such as the SS and LCC-S, ensures a stable output power when misalignment occurs [17], [18]. However, these methods may use many passive components, leading to extra power loss and necessitating intricate parameter design. Third, the closed-loop controller, which is essential for the WCS, ensures an accurate output power adjustment when misalignment occurs. In [19], a fractional-order WCS that has high misalignment tolerance is designed. In [20], a primary side dc–dc converter is proposed to adjust the output power when misalignment occurs. Without considering the use of the above complex magnetic coupler and compensation topology, this article will adopt the closed-loop control strategy to address the misalignment problem.

In terms of the ZVS state, it can be realized by the following methods: adjusting the inverter's operation frequency to be higher than the resonant frequency [21], [22]. However, this method may cause a bifurcation phenomenon that further leads to systematic instability. Switchable capacitor banks controlled by numerous relays also attain automatic impedance matching [23], [24]. However, this method should dynamically connect different quantities of capacitors to realize the desired value; many active switches and discrete capacitance tuning are used, which is undesirable for practical WCSs. A switch-controlled capacitor (SCC), whose capacitance is adjusted by controlling the switches' conduction times, also realizes dynamic tuning. In [25], the SCC with an active rectifier realizes the ZVS state for the inverter and the maximum system efficiency tracking. In [26], an SCC is applied in the LCC-S topology to achieve CC charging and ZVS state when the mutual inductance varies. However, since the SCC is directly connected to the resonant circuit, it may suffer from significant current or voltage stress, especially when the system power level is high.

Generally, the closed-loop control strategy for power control is classified into the primary and secondary sides, which have their characteristics [27]. The primary side type maximizes the receiver's compactness, such as using a dc–dc converter and phase-shift controlled full-bridge inverter [28], [29], [30]. However, once the secondary side charging information that is transferred via wireless communication fails, the WCS may malfunction. Although the secondary side type can avoid using wireless communication, it brings additional weight and volume to the receiver due to the usage of a power adjustment circuit, such as the active rectifier and dc–dc converter [31], [32], [33]. In this article, the receiver circuit should be as lightweight as possible, limited by the design requirement; then, the primary side type is chosen to realize the desired CP charging.

A single-stage inductive power transfer (IPT) converter, which operates as a wireless CP battery charger and maintains the maximum efficiency throughout the charging process, is proposed in [34]. An optimal control strategy of a single-stage IPT battery charger is used to achieve the maximum efficiency for CP charging [35]. In [36], a multiple Tx array architecture and circuit topology with the current phase shift modulation technique are proposed to realize CP charging. A self-tuning double-sided LCC WCS based on SCC is proposed to maintain fixed output power on the secondary side against self or mutual inductance variation of the magnetic coupler [37]. An optimal control strategy for the DLCC-SCC IPT system that realizes CP charging and zero phase angle under large misalignments is designed in [38]. In [39], a flexible CP range extension scheme with a self-oscillating WCS realized on the primary side is proposed for a drone. Combined with a comprehensive analysis of the above methods, this article further proposes a primary side circuit to realize the ZVS state and CP charging.

B. Main Works and Contributions

This article's research originates from an engineering project focused on designing a WCS for AGVs and addressing two key technical challenges encountered during its practical operation. The work involves creating an "all-in-one" type controllable magnetic flux capacitor (CMFC) on the WCS's primary side. Then, it not only solves the problems analyzed above but also offers advantages over the two existing similar methods, which are detailed in the Appendix. Then, the main contributions of this article are summarized as follows.

1) From the viewpoint of hardware, the CMFC is designed based on a concept called the "controllable magnetic flux principle." The working principle and detailed parameter design method are thoroughly explained.
2) From the viewpoint of software, the closed-loop control strategy is proposed to ensure the CMFC works efficiently, achieves ZVS state for the full-bridge inverter, and CP charging for the battery. Besides, the detailed control flow of the WCS with CFMC is analyzed.

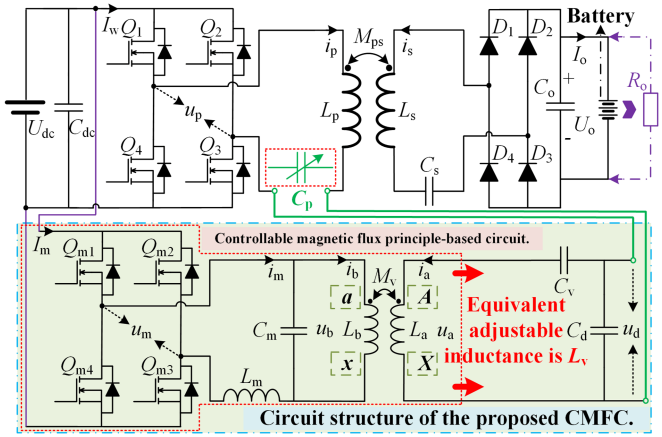

Fig. 2. Designed WCS for AGVs.

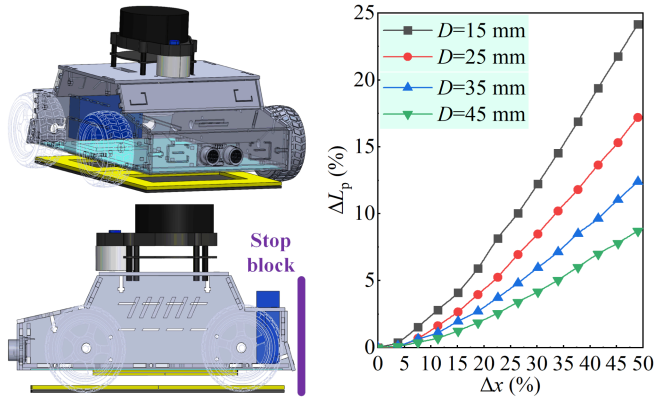

Fig. 3. Installation diagram of the DD-type magnetic coupler and simulation results of ΔL_p versus the x-direction misalignment distance.

3) From the method verification perspective, an engineering prototype is constructed and installed on the AGV, and then simulations and experiments verify the feasibility of the CMFC. Besides, its advantages and extension work are provided for future research.

The rest of this article is organized as follows. The circuit structure and existing problems of the WCS for AGV are given in Section II. The CMFC's working principle and parameter design method, which are this article's core innovation points, are illustrated in Section III. Section IV presents the closed-loop control strategy for the WCS with CMFC. Section VI verifies that the CMFC achieves the desired goals through experimental results and provides future work. Finally, Section V concludes this article.

II. Analysis of the Designed WCS for AGVs

First, a WCS, which uses the combination method of primary side circuit-based power control and detuned SS-compensation, is designed for AGVs. Second, two core technical problems that usually exist and should be solved in this kind of WCS are explored via theoretical analysis and simulation verification.

A. Circuit Structure Analysis

As shown in Fig. 2, the WCS's primary side circuit consists of a full-bridge inverter (MOSFETs Q_1–Q_4) and a resonant tank (transmitter coil L_p and equivalent capacitor C_p realized by the proposed CMFC). Then, the CMFC, which is covered by the light green box, consists of a full-bridge inverter (MOSFETs Q_{m1}–Q_{m4}), an LC-type filter (inductor L_m and capacitor C_m), a transformer (primary and secondary side coils L_a and L_b, whose mutual inductance is M_v), a capacitor C_v serially connected with L_a, and a capacitor C_d parallelly connected with L_a and C_v. The CMFC is then serially connected to L_p. The input and output voltages of the CMFC's full-bridge inverter are U_{dc} and u_m, respectively. The currents that flow through the transformer's primary and secondary sides are i_a and i_b, respectively. Note: The proposed CMFC in the light green box, this article's core innovation point, is only used for power adjustment and does not transfer power to the battery.

The WCS's secondary side consists of a resonant tank (receiver coil L_s and capacitor C_s), a full-bridge rectifier (diodes D_1–D_4), a filter (capacitor C_o), and a battery (equivalent load resistance is R_o). The input and output voltages of the full-bridge inverter are U_{dc} and u_p, respectively. The currents that flow in the primary and secondary side resonant tanks are i_p and i_s, respectively. Then, the mutual inductance of the WCS's magnetic coupler is M_{ps}. The system working process is analyzed below: the charging current I_o and voltage U_o, whose product is the charging power P_o, are sent to the primary side by wireless communication. The primary side controller adjusts C_p to realize the CP charging for the battery and ZVS state for the full-bridge inverter when M_{ps}, L_p, and R_o vary.

B. Technical Problems Analysis

Problem one: The magnetic coupler's misalignment not only affects the mutual inductance but also may seriously affect the transmitter coil's self-inductance, thereby causing a non-ZVS state for the full-bridge inverter, which deteriorates the WCS's operating performance.

Considering the structure of the AGV, the magnetic coupler's receiver is usually placed beneath the iron chassis of the AGV, as shown in Fig. 3. After researching the distance between the chassis of light-load AGVs and the ground, this value is smaller than 55 mm. Then, the actual magnetic coupler's transmission distance D in this article is determined based on the following analysis. As shown in Fig. 3, assuming that the thicknesses of the magnetic coupler's transmitter and receiver enclosures are all 10 mm, D is set to be 35 mm to balance the reduction of L_p versus Δx, where Δx and ΔL_p are expressed as in (1). x_i is the ith x-direction misalignment distance and L_p is L_{pi} ($i = 0, 1, 2, 3, \ldots$). Δy and ΔP_o use the same rule. The influence of the reduction of L_p on WCS's operating performance is analyzed below.

$$\Delta x = \frac{x_i}{x_0} \cdot 100\%; \Delta L_p = \left(1 - \frac{L_{pi}}{L_{p0}}\right) \cdot 100\%. \quad (1)$$

Taking into account the design requirements of the WCS's parameters, the coil turns of the magnetic coupler's transmitter (N_T, single layer) and receiver (N_R, double layer) are optimized

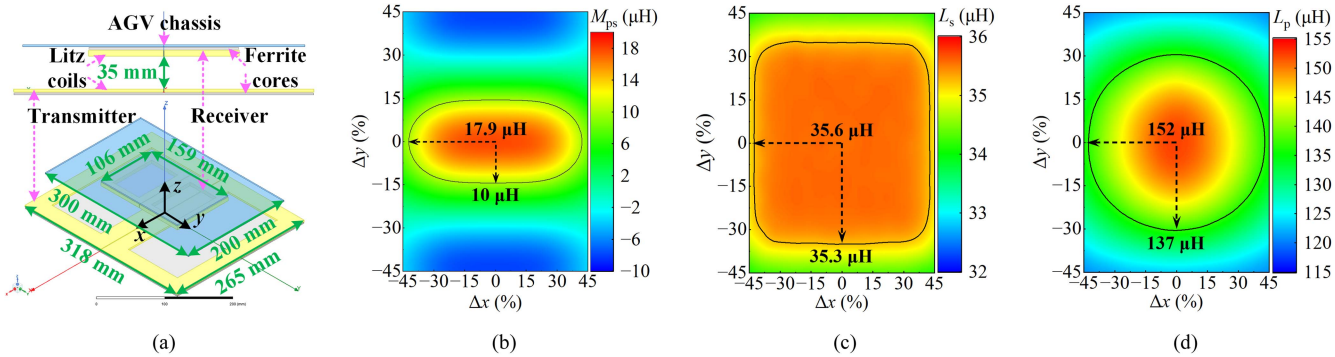

Fig. 4. Analysis of the optimized magnetic coupler. (a) Simulation model. (b) M_{ps}. (c) L_s. (d) L_p.

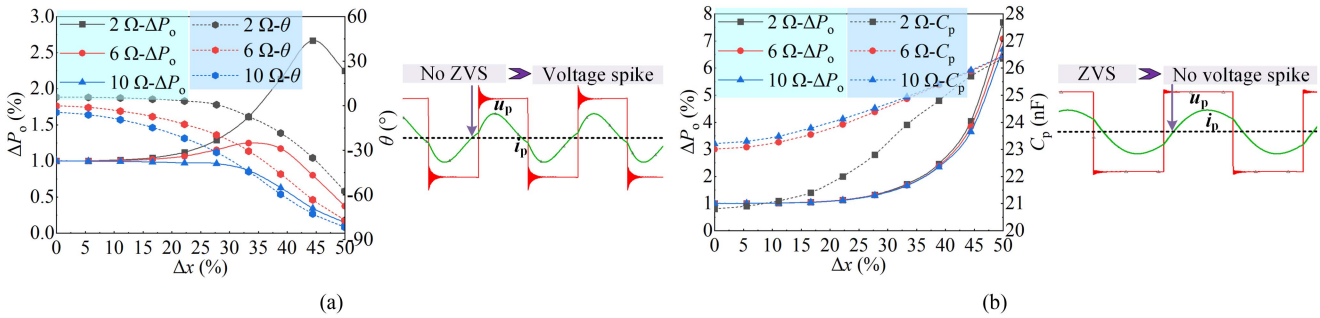

Fig. 5. Simulation results when misalignments occur. (a) θ and P_o when C_p is a fixed value to compensate for L_{p0}. (b) θ and P_o when C_p is an adjustable value to compensate for L_{pi}. Note: positive and negative signs of θ indicate the inductive and capacitive impedance of the primary side, respectively.

as 9 and 4, respectively. Meanwhile, the ferrite cores with PC95 material (50 mm × 50 mm × 2.5 mm) and Litz wire of 0.05∗1000 strands construct the magnetic coupler. Then, Fig. 4(a) shows the detailed parameters of the magnetic coupler.

In terms of the installation of the magnetic coupler's receiver, Fig. 4(b) gives guidance: the fluctuation of M_{ps} is stable in the x-direction, corresponding to a strong antimisalignment ability. Hence, the magnetic coupler's receiver is mounted on the AGV according to Fig. 3. A stop block is then placed behind the AGV to limit its y-direction misalignment. Then, even when the AGV is located above the magnetic coupler's transmitter and there is an x-direction misalignment, it can still ensure a high WCS's operating performance. Besides, in terms of the influence of the magnetic coupler's misalignment on its coil's self-inductance, Fig. 4(c) indicates that L_s remains constant when misalignment occurs; however, due to the AGV chassis and the small D. Fig. 4(d) further confirms that L_p decreases along with the increase of the horizontal misalignment distance, which is a typical case in this kind of WCSs and should be solved urgently.

Equations (2) and (3) further indicate that this problem will induce the WCS's primary side impedance Z_p to be capacitive, which further influences the ZVS state for the full-bridge inverter. When C_p is a fixed value, Fig. 5(a) verifies that the reduction of L_p will induce θ to be smaller than zero, corresponding to the capacitive impedance of the primary side resonant tank. Then, the full-bridge inverter will suffer from large voltage spikes and power loss. In contrast, Fig. 5(b) shows that P_o is much larger than Fig. 5(a) by employing a suitable C_p to compensate for the reduction of L_p, which the proposed CMFC realizes in this article. Besides, Fig. 5(b) shows that when θ is larger than zero, corresponding to a ZVS state for the full-bridge inverter, the voltage spike is eliminated significantly.

$$Z_p = \frac{(\omega M_{ps})^2 \pi^2}{8R_o} + j\frac{\Lambda}{\omega C_p}, \Lambda = \omega^2 L_p C_p - 1 \tag{2}$$

$$\theta = \arctan\frac{8R_o\Lambda_1}{\omega C_p(\omega M_{ps})^2\pi^2} \Rightarrow \begin{cases} \Lambda > 0, Zp \text{ is inductive} \\ \Lambda < 0, Zp \text{ is capacitive} \end{cases}. \tag{3}$$

On the above basis, it is confirmed that the compensation for the reduction of L_p to ensure a ZVS state for the full-bridge inverter is still necessary. Therefore, this article presents a new solution from the viewpoint of circuit topology innovation.

Problem two: The inevitable variation of the transmitter coil's self-inductance and mutual inductance of the magnetic coupler, as well as the battery's equivalent load resistance, influences the charging power, thereby requiring closed-loop control to achieve the desired charging goal for the WCS.

The root mean square (RMS) value of i_p is further given by

$$I_p = \frac{16\sqrt{2}U_{bus}R_o(\omega C_p)}{\pi\sqrt{64R_o^2\Lambda^2 + \pi^4(\omega C_p)^2(\omega M_{ps})^4}}. \tag{4}$$

Then, P_o, which is deduced as (5), further confirms that a controllable C_p can regulate P_o to the desired one even when L_p, M_{ps}, and R_o vary. Meanwhile, it points out that the ZVS state for the full-bridge inverter should always be realized to

TABLE I
MAIN PARAMETERS OF THE DESIGNED WCS WITH CMFC

Symbol	Parameter note	Value
U_{bus}	System input direct voltage	150 V
f	System operating frequency	85 kHz
L_p and L_s	The transmitter and receiver coils' rated self-inductance (WCS)	152 μH and 36 μH
M_{ps}	Magnetic coupler's rated mutual inductance	17.8 μH
C_v	The series capacitor's value	10 nF
C_d	The parallel capacitor's value	20 nF
L_a and L_b	The transmitter and receiver coils' rated self-inductance (CMFC)	240 μH and 280 μH
M_v	Transformer's rated mutual inductance (CMFC)	235 μH
L_m and C_m	Inductance and capacitance of the LC-type filter (CMFC)	90 μH and 40
P_o	Battery charging power	350 W
R_o	The equivalent load resistance of the battery during CP charging	2.57–8.33 Ω

ensure the highly efficient operation of the WCS. As a remark, this article uses the primary side circuit and control method to discover the power adjustment, but not the secondary side one, to avoid the extra weight and space occupancy rate of the AGV.

$$P_o = \frac{64R_oU_{bus}^2(\omega C_p)^2(\omega M_{ps})^2}{64R_o^2\Lambda^2 + \pi^4(\omega C_p)^2(\omega M_{ps})^4}. \quad (5)$$

Furthermore, a solution to the above problems, which are the ZVS state and CP charging realization, is still to be urgently explored. Based on the literature research, although two types of methods, which are classified into the circuit topology and impedance adjustment, can also solve these problems, they may suffer from the following issues:

As indicated by case I in Table II in the Appendix, although the combination of a duty cycle-controlled dc–dc converter and a frequency-controlled full-bridge inverter can achieve this article's goals, it negatively influences the system efficiency and secondary-side resonant state [40]. Meanwhile, considering the first problem in this article, when the inevitable reduction of L_p occurs, the WCS's available frequency adjustment range may be limited. Besides, it may also be a challenging task to precisely synchronize the dc–dc converter's duty cycle with a full-bridge inverter's frequency from the viewpoint of control strategy. In other words, the WCS usually desires the fewer the control variables, the better, thereby reducing the complexity of control. The method in case I cannot meet this requirement.

As shown in case II in Table II in the Appendix, although the SCC can achieve the article's goals with a simple circuit, its power elements may usually endure higher voltage or current stress, thereby increasing the complexity and cost of the power device options, particularly at high power levels [41], [42], [43]. The experimental results in the Appendix confirm this statement. Hence, combined with a substantial literature review, it points out that the structural complexity and system design goals of the WCS may usually be mutually restrictive [44], [45], [45]. In other words, a balance between these two aspects is required in the WCS's design, which further guides this article's research work.

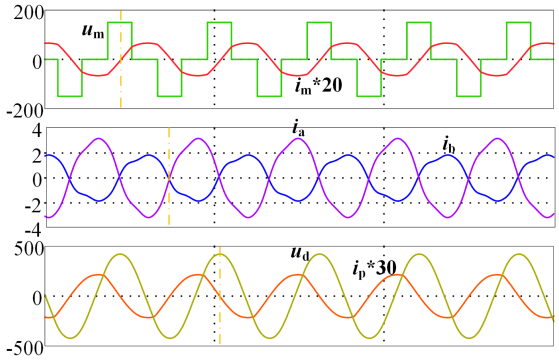

Fig. 6. Working waveforms of the CMFC.

Based on the comprehensive analysis of the advantages and disadvantages of the above two methods, this article proposes a CMFC that avoids the problems that exist in these two methods and is based on the idea of "all-in-one problem solving," that is, to use a relatively simple circuit and algorithm to solve as many problems as possible.

III. DESIGN OF THE PROPOSED CMFC

The CMFC realizes the ZVS state for the full-bridge inverter and CP charging for the battery. Meanwhile, it also achieves the flexible tuning for the primary side resonant tank, which further reduces the difficulty of capacitor matching during the initial design stage of the WCS. Therefore, this section's core work detailly the working principle and parameter design method of the CMFC. Besides, the CMFC's key components, which are the LC-type filter and transformer, are optimized and verified by simulation results.

A. Working Principle Analysis

Based on Fig. 2, the CMFC's equivalent circuit is simplified into L_v, C_v, and C_d, where C_v and C_d have fixed capacitance values. L_v is adjusted by the circuit in the red dashed box based on the "controllable magnetic flux principle", which is further analyzed as follows: i_a is collected by a current transformer, and then used as a triggering condition to generate pulsewidth modulation (PWM) signals for the full-bridge inverter using a closed-loop control algorithm to ensure that i_m lags u_m by 90°. i_m flows through the LC-type filter, and then i_b achieves an opposite phase with the same frequency as i_a. On this basis, the magnetic fluxes that i_a and i_b generate cancel each other out, thereby affecting the working magnetic flux in the transformer through adjusting the ratio α between i_a and i_b, as shown in Fig. 6. Then, L_v is obtained between ports A and X. It points out that the CMFC's transformer differs from the one usually used in power electronics because it is actively excited on both sides with two currents that feature the same frequency and opposite phase, which is the basic reason why the CMFC's magnetic flux is regulated. Besides, Fig. 6 shows that the CMFC's full-bridge inverter operates at the ZVS state.

Based on the above principle and Fig. 7, the adjustment equation of L_v is further deduced as follows: the coil turns of the primary and secondary side winding in the CMFC's transformer

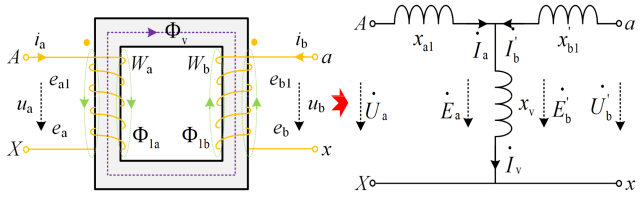

Fig. 7. Transformer model and its T-type equivalent circuit model.

are W_a and W_b, respectively. The leakage and excitation fluxes of the primary and secondary side windings are Φ_{a1}, Φ_{v1}, and Φ_{b1} and Φ_{v2}, respectively. The leakage circuit permeability and excitation circuit permeability are Λ_{a1} and Λ_{b1}.

$$\Phi_{a1} = \Lambda_{a1} W_a i_a; \Phi_{v1} = \Lambda_v W_a i_a; \Phi_{b1} = \Lambda_{b1} W_b i_b;$$
$$\Phi_{v2} = \Lambda_v W_b i_b \tag{6}$$

According to electromagnetic induction, the excitation and leakage potential of primary and secondary side windings are e_a, e_{a1}, e_b, and e_{b1}, respectively.

$$\begin{aligned} e_a &= -\left(W_a^2 \Lambda_v\right) \frac{di_a}{dt} - \left(W_a W_b \Lambda_v\right) \frac{di_b}{dt}, \\ e_{a1} &= -\left(W_a^2 \Lambda_{a1}\right) \frac{di_a}{dt} \\ e_b &= -\left(W_b^2 \Lambda_v\right) \frac{di_b}{dt} - \left(W_a W_b \Lambda_v\right) \frac{di_a}{dt}, \\ e_{b1} &= -\left(W_b^2 \Lambda_{b1}\right) \frac{di_b}{dt} \\ L_a &= W_a^2 \Lambda_{a1} + W_a^2 \Lambda_v; L_b = W_a^2 \Lambda_{a1} + W_b^2 \Lambda_v; \\ M_v &= W_a W_b \Lambda_v. \end{aligned} \tag{7}$$

Based on Kirchhoff's voltage law, the port voltage of the CMFC's transformer is deduced as (8), where the leakage inductances of the primary and secondary side windings are x_{a1} and x'_{b1}; the excitation inductance is x_v. n is the ratio of W_a and W_b, which is set to one or nearly one to simplify the analysis.

$$\begin{aligned} \dot{U}_a &= \left[j \underbrace{\omega \left(L_a - n M_v\right)}_{x_{a1}} \right] \dot{I}_a + j \underbrace{\omega n M_v}_{x_v} \left(\dot{I}_a + \frac{\dot{I}_b}{n} \right) \\ \dot{U}_b &= \left[j \frac{1}{n^2} \underbrace{\omega n \left(n L_b - M_v\right)}_{x'_{b1}} \right] \dot{I}_b + j \frac{\omega M_v}{n} \left(\dot{I}_b + n \dot{I}_a \right). \end{aligned} \tag{8}$$

Combined with Fig. 6, (7) is further given by

$$\dot{U}_a = j \left(x_{a1} + x_v\right) \dot{I}_a + j x_v \dot{I}'_b; \dot{U}'_b = j \left(x'_{b1} + x_v\right) \dot{I}'_b + j x_v \dot{I}_a$$
$$\dot{I}'_b = \dot{I}_b / n, \text{and } \dot{U}'_b = n \dot{U}_b. \tag{9}$$

Then, L_v is given by (11), where the value range of α depends on the L_v and M_v of the CMFC as long as L_v is larger than zero.

$$\dot{U}_a = j \left(x_{a1} + x_v\right) \dot{I}_a + j x_v \dot{I}'_b, \dot{I}'_b = -\alpha \dot{I}_a$$
$$\Rightarrow L_v = L_a - \alpha n M_v \overset{n \approx 1}{=} L_a - \alpha M_v \tag{10}$$

Based on Fig. 2, the CMFC's equivalent capacitance C_p is given by (11), which is this article's core equation for power regulation. As a remark, the above analysis confirms that the CMFC's working principle differs quite from the usually used impedance adjustment methods [41], [42], [43], and its advantages will be analyzed in the following sections. In other words, this article proposes a new type of impedance adjustment technique.

$$\begin{aligned} &\underset{\text{Capacitive impendance}}{\omega^2 L_v C_v < 1} : C_p = C_d + \frac{C_v}{1 - \omega^2 C_v \left(L_a - \alpha M_v\right)} \\ &\underset{\text{Inductive impendance}}{\omega^2 L_v C_v > 1} : L_x \\ &= \frac{\omega^2 C_v \left(L_a - \alpha M_v\right) - 1}{\omega^2 \left[C_v - C_d \left(\omega^2 C_v \left(L_a - \alpha M_v\right) - 1\right)\right]}. \end{aligned} \tag{11}$$

Fig. 8 confirms that C_p and L_v are adjusted by controlling α. Besides, Fig. 8(d) indicates that when L_v is larger than $1/(\omega^2 C_v)$, C_p will be smaller than zero, which corresponds to an inductive impedance. Hence, the CMFC's parameters should be suitably designed based on practical requirements. Note: This article only uses CMFC to realize capacitive impedance adjustment. The inductive impedance for the CMFC is also analyzed in the Appendix as an extension of this article's work.

B. Parameter Design Method Analysis

The value range of C_p should satisfy (12), whose minimum and maximum values are C_{pl} and C_{ph}, respectively. These two values are usually determined by considering the system design goals within a full range of parameter variation.

$$\begin{aligned} \underbrace{C_d + \frac{C_v}{1 - \omega^2 C_v L_a}}_{C_{pl}} &\le C_d + \underbrace{\frac{C_v}{1 - \omega^2 C_v \left(L_a - \alpha M_v\right)}}_{C_{vv}} \\ &\le \underbrace{C_d + \frac{C_v}{1 - \omega^2 C_v \left(L_a - M_v\right)}}_{C_{ph}}. \end{aligned} \tag{12}$$

Based on initial experiments, C_d is determined by two factors: it must be smaller than C_{pl} to ensure C_{vv} is positive, and it should be relatively large to minimize the working current of the CMFC, thereby reducing its power loss. With C_d set, the maximum C_v is derived from (13). Once C_d and C_v are fixed, the range of L_v is determined, with L_{vl} as the minimum and L_{vh} as the maximum.

$$\underbrace{\frac{1}{\omega^2 C_v}\left(1 - \frac{C_v}{C_{pl} - C_d}\right)}_{L_{vl}} \le L_v \le \underbrace{\frac{1}{\omega^2 C_v}\left(1 - \frac{C_v}{C_{ph} - C_d}\right)}_{L_{vh}} \overset{L_v > 0}{\Rightarrow}$$
$$C_v \le \left(C_{pl} - C_d\right) \overset{C_d \text{ and } C_v \text{ are dertermined}}{\Rightarrow} L_{vl} \le L_v \le L_{vh}. \tag{13}$$

Based on (13), L_a is further given by (14). For the CMFC's transformer, the ratio of L_b to L_a is γ to provide more design freedom (γ usually ranges from 1 to 1.2 based on experience). k is the coupling coefficient, which is generally larger than 0.9.

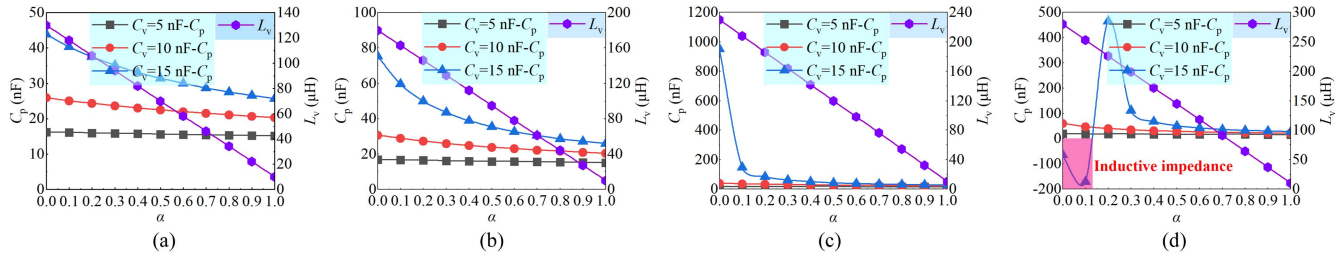

Fig. 8. Simulation results of C_p when C_d is 10 nF. (a) $L_a = 130$ μH and $M_v = 120$ μH. (b) $L_a = 180$ μH and $M_v = 170$ μH. (c) $L_a = 230$ μH and $M_v = 220$ μH. (d) $L_a = 280$ μH and $M_v = 270$ μH.

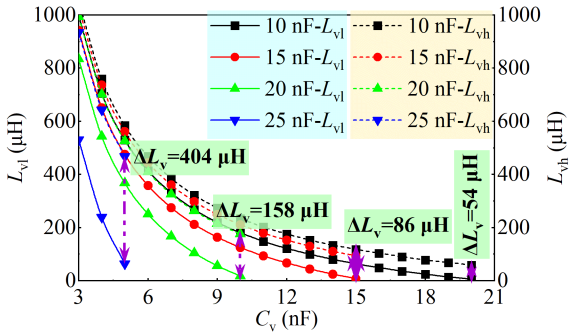

Fig. 9. Simulation results of L_v versus C_v when C_d varies.

Because multiple related parameters should be determined for the CMFC during the design process, (14) only gives the value range of L_a, but not the exact value. Then, empirical design and simulation iterations are further used to determine the final L_a. After determining C_d, C_v, L_a, and M_v, a suitable combination of L_m and C_m is chosen to achieve a resonant frequency of 85 kHz. This combination suppresses high-frequency ripple from the CMFC's full-bridge inverter, ensuring optimal performance.

$$\frac{L_{vl}}{1-\alpha k\sqrt{\gamma}} \le L_a \le \frac{L_{vh}}{1-\alpha k\sqrt{\gamma}} \overset{L_a \text{is dertermined}}{\Rightarrow} M_v = k\sqrt{\gamma}L_a. \tag{14}$$

Combined with Table I, the value of C_p should range from 30.5 to 38 nF to ensure the system design goals. As shown in Fig. 9, when C_v is larger than 20 nF, the value range of L_v is so large that it will cause more power loss because of the inherent resistance. When C_v is smaller than 20 nF, the value range of L_v becomes small and may not meet the required value range of C_p. Then, C_d is set to 20 nF in this article, which is realized by two capacitors of 10 nF connected in parallel.

In general, these two capacitors are used because they can be easily obtained from existing capacitor models. Otherwise, take C_d as 18 nF, which meets the analysis in Fig. 9, as an example; it should be constructed by multiple capacitors in series/parallel without customization, increasing the complexity. Furthermore, based on (13) and Fig. 9, C_v, which should be smaller than 10.5 nF, is set to 10 nF, using a similar reason as selecting C_d. Then, L_v ranges from 16.5 to 175.5 μH.

Based on (14) and assuming that k and γ equal 0.91 and 1.2, L_a should be larger than 190 μH to ensure the desired value range of C_d, as shown in Fig. 10(a). Besides, considering that the capacitance drift caused by the temperature and tuning error may influence the CMFC's working performance in practical applications [42]. This article takes the worst case of C_v, C_d, and C_m fluctuating -10%–$+5\%$ as an example. L_a is then further optimized, and L_a is set to 230 μH, as shown in Fig. 10(c).

C. Integration of the CMFC's Inductive Elements

Fig. 11 shows that the CMFC's transformer and L filter can be integrated to ensure a compact structure using the orthogonal flux method, which avoids the cross-coupling effect between the CMFC's transformer and L filter. Based on the parameters designed in Section III-B, when the Litz wire is 0.05 × 600 strands, the optimized coil turns of L_a (single layer), L_b (single layer), and L_m (double layer) are 10, 10, and 12, respectively.

Fig. 12 further verifies the CMFC's working principle. When α increases, the magnetic induction intensity of ferrite cores in the transformer decreases, corresponding to the decrease of L_v. It also confirms that the CMFC differs from the SCC.

IV. Analysis of the Closed-Loop Control Strategy

Section III details the CMFC's circuit from the hardware perspective. This section will illustrate the closed-loop control strategy for the designed WCS from a software perspective, so as to ensure the completeness of the CMFC's research. Besides, simulation results validate the CMFC's feasibility.

A. Control Strategy

As shown in Fig. 13, the closed-loop control strategy's block diagram mainly consists of two parts: one for the operation of CMFC and the other for the realization of ZVS state and CP charging. Combined with the current and voltage sensors, I_o and U_o are multiplied and transferred to the primary side PI controller for the CP charging through wireless communication. On the one hand, the PI controller's output is transferred to the PWM signal generation circuit. On the other hand, i_a is processed by a signal synchronizing circuit to generate a signal that ensures i_b is in the opposite phase and has the same operating frequency as i_a. Then, this signal is also transferred to the PWM signal generation circuit. Finally, four PWM signals, whose phase-shift angle can be adjusted, will be used by the full-bridge inverter to regulate α to achieve the desired C_p for realizing the ZVS state and CP charging.

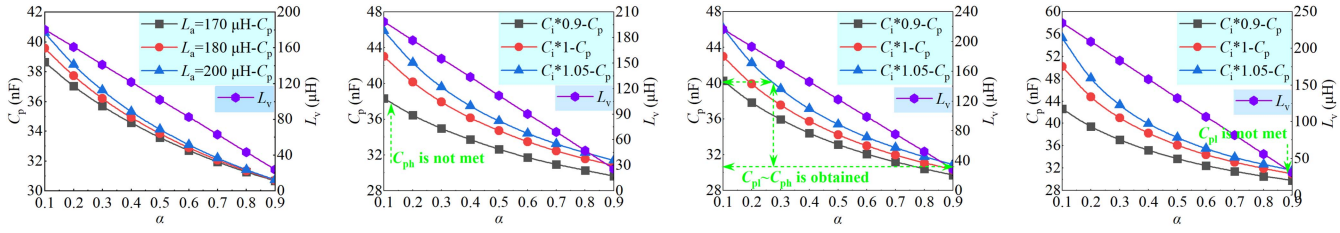

Fig. 10. Simulation results of L_v versus α. (a) L_a ranges from 180 to 200 μH. (b) $L_a = 220$ μH. (c) $L_a = 240$ μH. (d) $L_a = 260$ μH. Note: (a) Corresponds to C_i (i = d, v, m), which has no value drift. (b)–(d) Corresponds to C_i that has value drift.

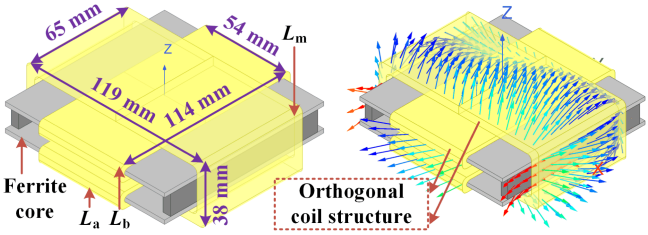

Fig. 11. Simulation model of the transformer and L filter in the CMFC.

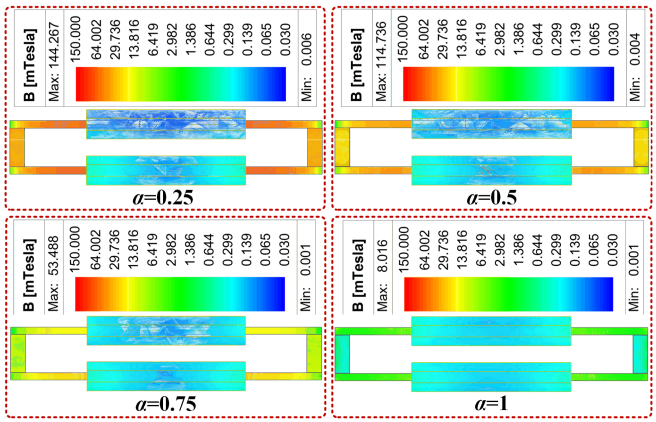

Fig. 12. Magnetic field distribution of the transformer under different α.

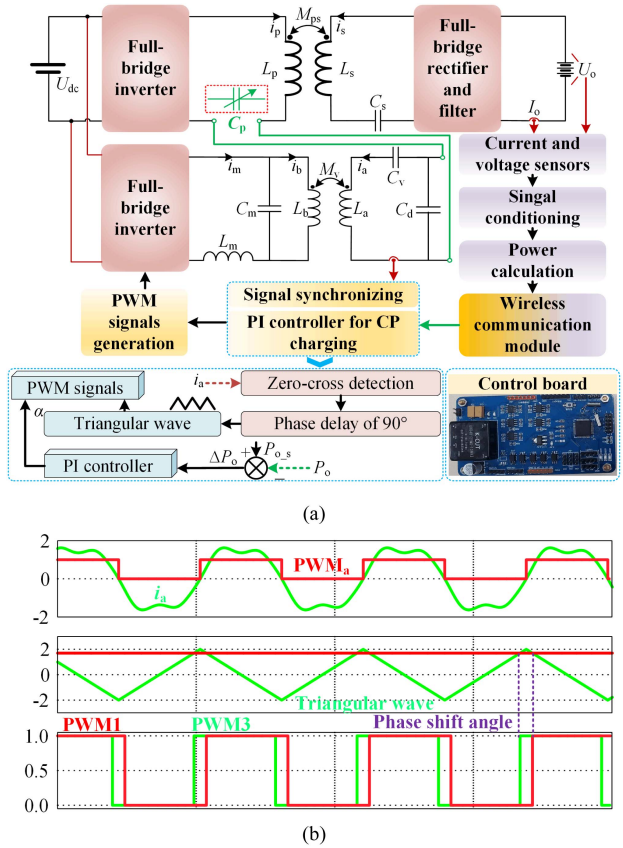

Fig. 13. Closed-loop control strategy. (a) Block diagram. (b) Waveforms.

B. Simulation Results

Considering the practical parameter drifts in the CMFC, 0% and −10% fluctuation of C_i is used as an example to validate the feasibility of the closed-loop control strategy, as shown in Fig. 14. When M_{ps} is 12.3 μH, the dynamic waveforms in Fig. 15 indicate that the ZVS state and CP charging are achieved using the closed-loop controlled CMFC.

V. Experimental Validation

Based on the above analysis, an experimental setup in Fig. 16 is built using Table I. Then, experimental results verify the CMFC's feasibility. Note: the CMFC, which is a primary side control circuit, can be applied to other applications, such as the uncrewed aerial vehicle; this article only takes the AGV as an example. The core motivation is to propose and design a CMFC that has better comprehensive performance compared to similar existing impedance adjustment circuits, such as SCC.

A. Experimental Setup Design

As shown in Fig. 16, the primary side full-bridge inverter consists of four single-channel MOSFET gate drivers from Infineon (1EDI60N12AF) and SiC MOSFETs from Wolfspeed (C2M0040120D). The compensation topology uses some low internal resistance capacitors from DAWNCAP. The rectifier uses four Schottky diodes from SIRECT (MBR60200PT). The waveforms are captured using an oscilloscope (SDS2204X) from SIGLENT. The inductances of the magnetic coupler are measured with an *LCR* analyzer (IM3536) from HIOKI. The system efficiency is measured by the power analyzer (WT1800) from HIOKI. The power supply N8944A from KEYSIGHT is used as the dc input source. The electronic load IT8514C+ from YOKOGAWA is used as the load during the system test stage.

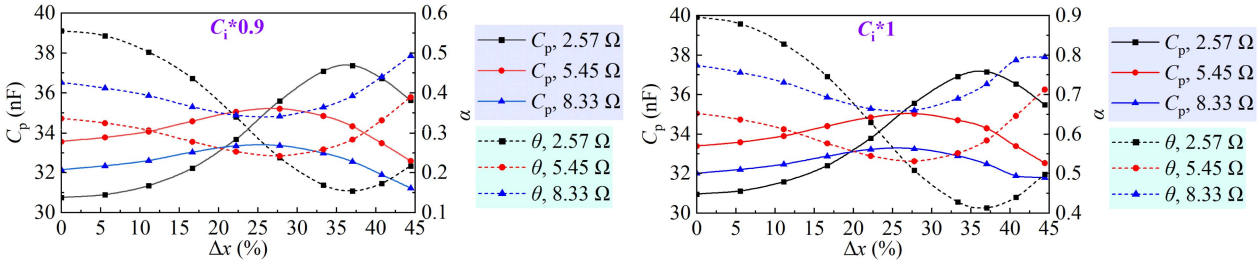

Fig. 14. Simulation results of C_p and α when R_o and M_{ps} vary.

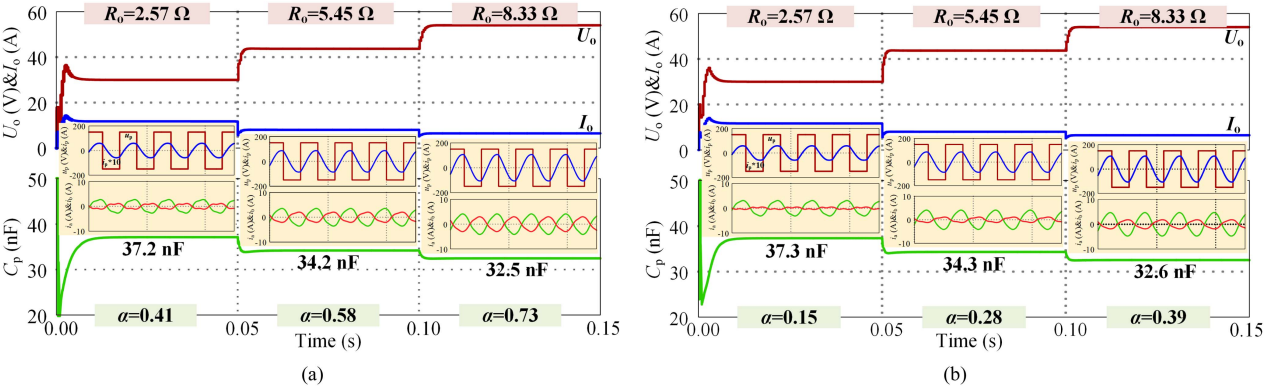

Fig. 15. Simulation waveforms during CP charging. (a) No parameter drift occurs in the CMFC. (b) Parameter drift of -10% occurs in the CMFC.

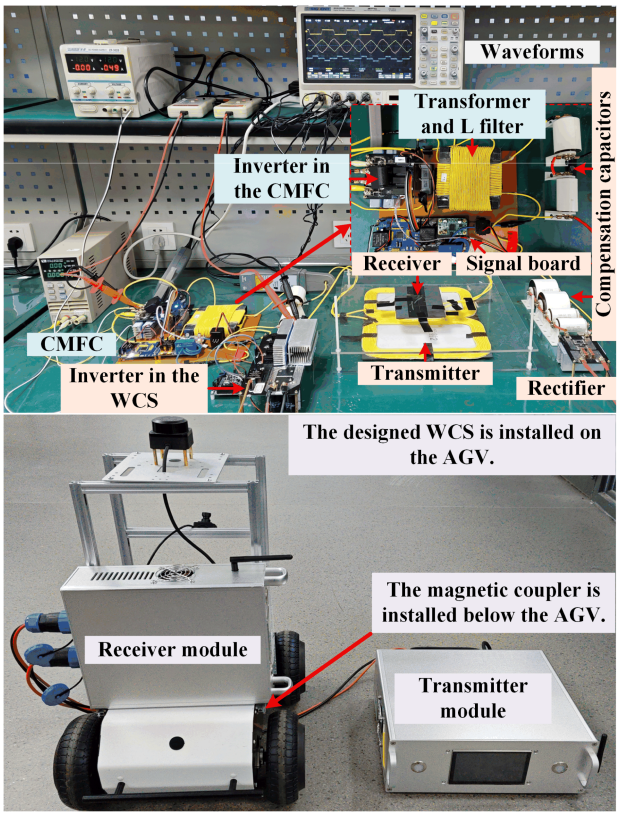

Fig. 16. Experimental setup of the WCS for AGVs.

Besides, a lithium-iron phosphate battery (30–54 V) is used as the load during the actual application stage.

B. Experimental Results Analysis

Fig. 17(a) validates that the carefully constructed magnetic coupler has good x-direction antimisalignment ability. In this article, the average error between the measured and simulated M_{ps} is less than 1.2% when the simulation model is calibrated with the actual prototype. When misalignment occurs, Fig. 17(b) gives the controllable region for CP charging. The blank area indicates that the CMFC can no longer work.

When C_i fluctuates, Fig. 18 verifies that CP charging can still be achieved by adjusting α. Besides, Fig. 18 shows that when C_i fluctuates by +5%, α may be larger than one to ensure a suitable C_p. For this case, L_v is smaller than 0, which indicates that the impedance of the CMFC's transformer (seen in ports A and X) is capacitive and is further analyzed in the Appendix. Note: (55, 35) indicates that the x- and y-direction distances are 55 mm and 35 mm, respectively. Other cases share the same rule.

As shown in Fig. 19(a), η decreases slightly within a suitable misalignment range; the maximum Δx reaches 33% to ensure that η exceeds 90% when R_o varies and no y-direction misalignment occurs. Fig. 19(b) shows that the CMFC's power loss accounts for one-fifth of the system power loss. Besides, all the CMFC's power losses are covered during the test, such as the auxiliary circuit's power loss (controller, driving circuit, and so on). Note: The results are the average values obtained from multiple measurements to ensure their reliability.

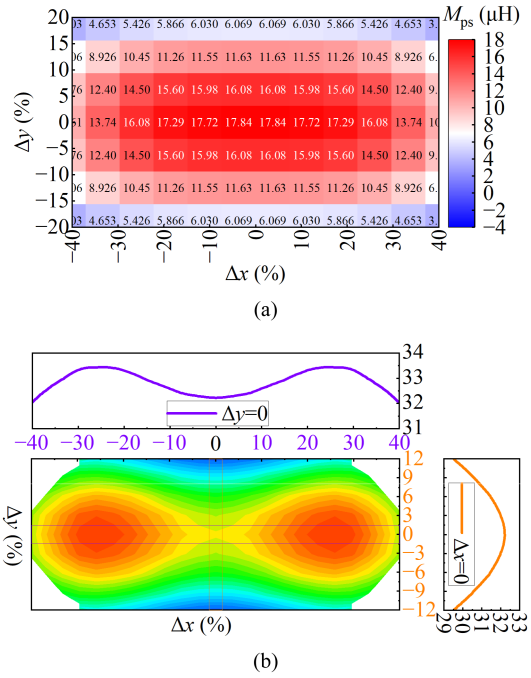

Fig. 17. Experimental results. (a) Measured M_{ps}. (b) Required C_p for CP charging when R_o is 8.33 Ω and no parameter drift in the CMFC.

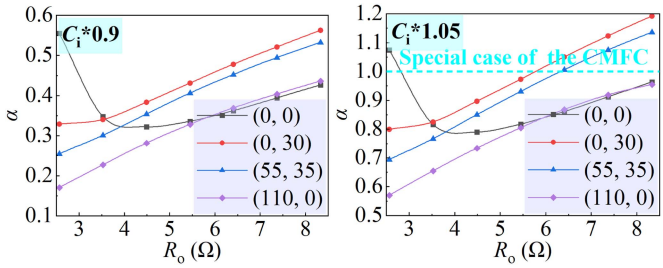

Fig. 18. Experimental results during CP charging.

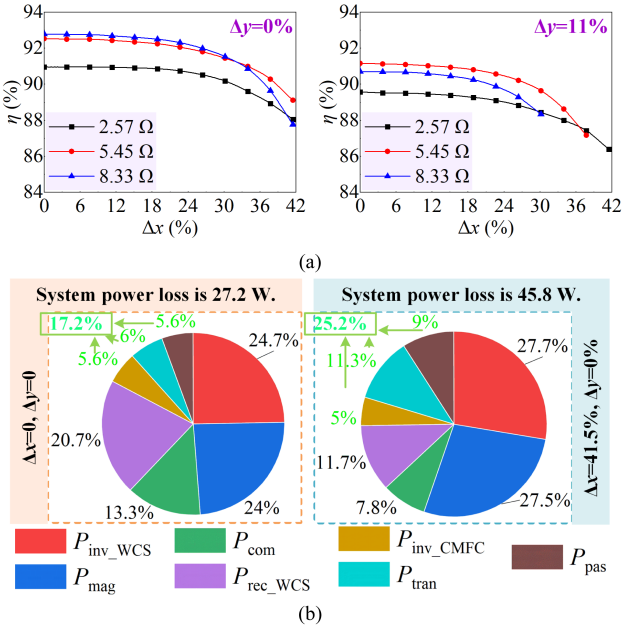

Fig. 19. Experimental results during the CP charging. (a) System efficiency. (b) Power loss distribution when R_o is 8.33 Ω. P_{inv_WCS}, P_{com}, P_{mag}, and P_{rec_WCS} are the power loss of the WCS's inverter, compensation capacitors, magnetic coupler, and rectifier, respectively. P_{inv_CMFC}, P_{tran}, and P_{pas} are the power loss of the CMFC's inverter, transformer, and passive components, respectively.

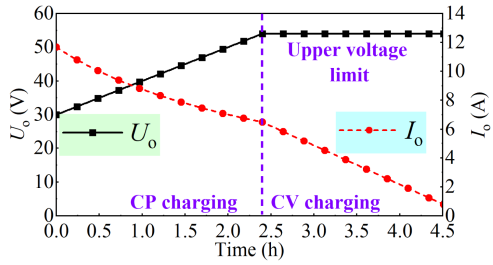

Fig. 20. Experimental results of the practical battery CP charging.

The battery CP charging curve is plotted in Fig. 20. When U_o reaches the upper limit, the CV charging is used to replenish the energy entirely. Note: if only quick charging is required, the charging process can be terminated once the upper voltage limit is met, and then the CV charging may not be essential because it usually takes a long time.

As shown in Fig. 21, the distortion of the current waveform does not affect the CMFC's operation. The dynamic regulation time is at the millisecond level when the parameters of the PI controller are optimized. Fig. 21 also shows that the CMFC usually uses a small current to maintain its operation, which is an advantage compared to the commonly used SCC, which may withstand large current stress and is analyzed in the Appendix.

C. Explanations and Future Work of This Article's Work

This article's work comes from an actual engineering project, which faces two technical problems analyzed in Section II-B. By analyzing the solutions presented in the existing literature, this article further proposes a new type of primary side power circuit, which is called the CMFC. Its design is based on a new concept of "controllable magnetic flux principle" that has not been further analyzed in the existing WCS. In other words, this article not only designs a WCS that meets an actual engineering project, which guides the relevant researchers, but also solves key issues that exist in this kind of WCS from the perspective of academic research. Finally, this article can be further regarded as scientific research derived from the engineering project. Furthermore, a comprehensive review of references indicates that when the WCS aims to achieve multiple goals, its control strategy and circuit complexity are usually high. Hence, it is necessary to consider a balance when designing the WCS. On this basis, although the CMFC has a relatively complex circuit structure, it not only achieves three design goals but also avoids problems in existing similar control methods.

As an extension of this article's work, the CMFC's control method and circuit structure can be optimized to enhance its adjustment range and reduce power loss, such as simplifying the inverse current generation circuit and designing a more compact transformer. The proposed CMFC, which is regarded as a new power adjustment circuit, can realize other functions,

Fig. 21. Experimental waveforms during the dynamic charging process. (a) $\Delta x = 0$ and $\Delta y = 0$. (b) $\Delta x = 37.7\%$ and $\Delta y = 0$.

such as CC/CV charging and dynamic tuning, which have been preliminarily verified and will be the subject of future research.

VI. Conclusion

This article explores the two core technical problems faced during the design of the WCS for AGVs, and proposes a CMFC to solve them. The closed-loop controlled CMFC on the WCS's primary side realizes the ZVS state for the full-bridge inverter and CP charging for the battery, along with the variation of the transmitter coil's self-inductance and the magnetic coupler's mutual inductance, and the battery's equivalent load resistance. Besides, it also avoids the matching difficulty of the resonant capacitor for the primary side resonant tank in the traditional mode. The circuit structure and working principle of the WCS are analyzed. Then, the two core technical problems need to be solved are analyzed through theoretical analysis and simulation verification. Compared with two existing methods that address these issues, the CMFC avoids their drawbacks while achieving the same goals. A detailed analysis of the CMFC's working principle, which is called the "controllable magnetic flux principle," and parameter design method, which is based on multiple formulas to determine the parameter value range, is provided. Combined with the CMFC, its closed-loop control strategy is analyzed and verified by simulations. Finally, an experimental setup is built. When the equivalent load resistance varies from 2.57–8.33 Ω, experimental results verify that the designed WCS for AGVs achieves 350-W CP charging and a maximum system efficiency of 92.7% when the misalignment distance in x- or y-direction is within 40% or 10% of the transmitter coil's width, respectively.

Appendix

A. CMFC's Inductive Impedance Realization

Two conditions that determine whether the CMFC realizes a capacitive or inductive impedance are illustrated as follows: When the CMFC has an inductive impedance, it can still adjust

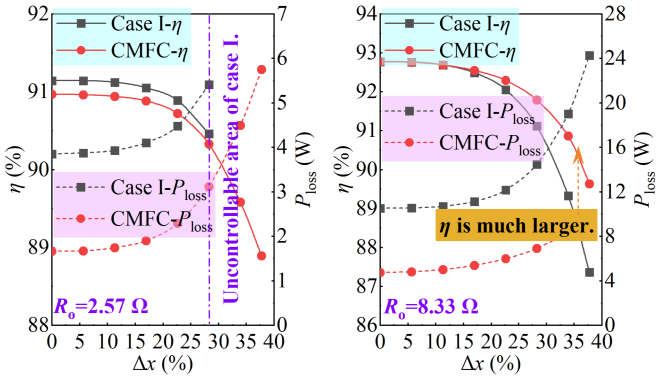

Fig. 22. Experimental data comparison between the CMFC and case I.

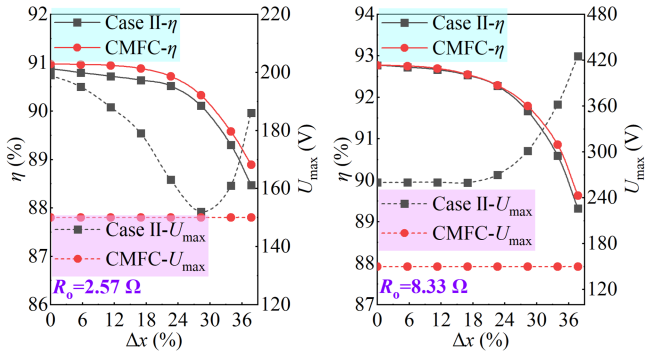

Fig. 23. Experimental data comparison between the CMFC and case II.

the charging power by designing its parameters suitably. In other words, the CMFC provides a relatively comprehensive method for impedance regulation.

1) Condition One: Assuming that L_a and M_v are fixed values and C_v uses different values, the equation that determines the critical point of capacitive impedance or inductive impedance is given by (A1). Along with the variation of α, when the minimum value of L_v is larger than $1/(\omega^2 C_v)$, the CMFC has an inductive impedance; when the maximum value of L_v is smaller than $1/(\omega^2 C_v)$, the CMFC has a capacitive impedance.

$$\begin{cases} L_{v\_min} = (L_a - M_v) > \frac{1}{\omega^2 C_v}, \text{inductive impedance} \\ L_{v\_max} = L_a < \frac{1}{\omega^2 C_v}, \text{capacitive impedance} \end{cases}. \tag{A1}$$

2) Condition Two: Assuming that C_v is a fixed value, and L_a and M_v choose different values, the equation that determines the critical point of capacitive impedance or inductive impedance is given by (A2). Along with the variation of α, when C_v is larger than $1/(\omega^2(L_a\text{-}M_v))$, the CMFC has an inductive impedance; when the maximum value of L_v is smaller than $1/(\omega^2 L_a)$, the CMFC has a capacitive impedance.

$$\begin{cases} C_v > \frac{1}{\omega^2 L_{v\_min}}, \text{inductive impedance} \\ C_v < \frac{1}{\omega^2 L_{v\_max}}, \text{capacitive impedance} \end{cases}. \tag{A2}$$

B. Power Loss Calculation of the WCS with CMFC

The WCS's power loss mainly comes from the full-bridge inverter, passive elements (the WCS's magnetic coupler and compensation capacitor, the CMFC's transformer and *LC*-type filter, and the extra series/parallel connected capacitor), and the full-bridge rectifier [47], [48]. Then, the power loss equations are deduced to assist in reducing power loss during the system design process. Besides, it points out that some other power losses that are not easy to calculate by the equation are not analyzed here, such as the power loss of connecting parts and printed circuit boards.

1) Power Loss Equation of the Full-Bridge Inverter: In this article, the full-bridge inverter in the WCS operates at the ZVS state, and the power loss equation is given by (A3), where the MOSFET's conduction loss, the antiparallel diode's conduction loss, and the full-bridge inverter and its antiparallel diodes' switching loss are expressed as (A4), (A5), and (A6), respectively. I_1 is the RMS value of the full-bridge inverter's output current, r_m is the drain-source on-state resistance, δ_d is the deadtime of the PWM driving signals, β is the primary side impedance angle, α is the phase-shift angle, r_{id} is the equivalent on-state resistance of the antiparallel diode, V_{if} is the forward voltage of the antiparallel diode, and E_{ON} and E_{OFF} are the turn-ON and turn-OFF energy losses of the MOSFET, respectively. V_{DD} and I_D are the reference drain-source voltage and source current of the MOSFET, respectively. Q_{DD} and I_{R_D} are the reverse voltage charge and reference current of the diode, respectively.

$$P_{Inverter} = P_{mos} + P_{diode} + P_{sw} \tag{A3}$$

$$P_{mos} = \frac{1}{\pi} I_1^2 r_m \left[\pi - \delta_d + \frac{1}{2}(\sin(\alpha+2\beta-2\delta_d) - \sin(\alpha+2\beta))\right] + \frac{1}{\pi} I_1^2 r_m \left[\pi - \delta_d + \frac{1}{2}(\sin(\alpha-2\beta) - \sin(2\beta-2\delta_d-\alpha))\right] \tag{A4}$$

$$P_{diode} = \frac{\sqrt{2}}{\pi} V_{if} I_1 \left[\sin\left(\delta_d - \frac{\alpha}{2} - \beta\right) + \sin\left(\frac{\alpha}{2} + \beta\right)\right] + \frac{\sqrt{2}}{\pi} V_{if} I_1 \left[\sin\left(\delta_d + \frac{\alpha}{2} - \beta\right) + \sin\left(\frac{\alpha}{2} - \beta\right)\right] + \frac{1}{\pi} r_{id} I_1^2 \left[\delta_d + \frac{1}{2}\sin(2\delta_d - \alpha - 2\beta) + \sin(\alpha+2\beta)\right] + \frac{1}{\pi} r_{id} I_1^2 \left[\delta_d + \frac{1}{2}\sin(2\delta_d + \alpha - 2\beta) + \sin(2\beta-\alpha)\right] \tag{A5}$$

$$P_{sw} = 2\sqrt{2} V_{dc} I_1 \left[\left|\cos\left(\frac{\alpha}{2} - \beta\right)\right| + \left|\cos\left(\frac{\alpha}{2} + \beta\right)\right|\right] \times \left(\frac{E_{OFF}}{V_{DD} I_D} + \frac{Q_{DD}}{I_{R\_D}}\right) f. \tag{A6}$$

2) Power Loss Equation of Passive Elements: In terms of passive elements, the power loss equation is given by (A7), where V_{av} and V_{bv} are the ferrite core volumes used by the primary and secondary sides of the transformer. B_a and B_b are the primary and secondary sides of the peak magnetic flux density. The Steinmetz coefficients k, c, and e related to the core material are obtained from manufacturer datasheets. Some low-power loss ferrite cores, such as PC95, are potential candidates for the WCS. In this article, the transformer uses the MnZn ferrite core with PC95 material. The coefficients of this core material are $k = 0.00925$, $c = 1.86$, and $e = 3.03$. V_m is the ferrite core volume

TABLE II
COMPARISON BETWEEN THE CMFC AND TWO EXISTING SIMILAR METHODS

Case	Power adjustment circuit diagram	Circuit structure covered by the light blue box	Control variable
I	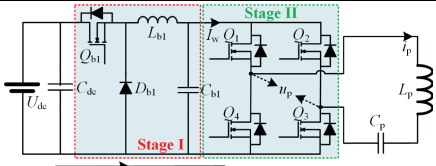	Buck converter and variable frequency-controlled full-bridge inverter. **Number of circuit components:** Four MOSFETs, one diode, one inductor, and two capacitors.	**The duty cycle** of the Buck converter and the **operating frequency** of the full-bridge inverter. By collecting i_p and u_p synchronizing the PWM signal.
II	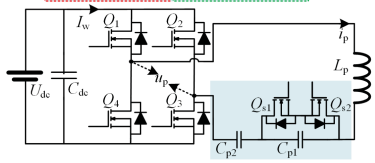	SCC. **Number of circuit components:** Two MOSFETs and capacitors.	**The duty cycle** of the CMFC's two MOSFETs. By collecting i_p to synchronize the PWM signal.
This article	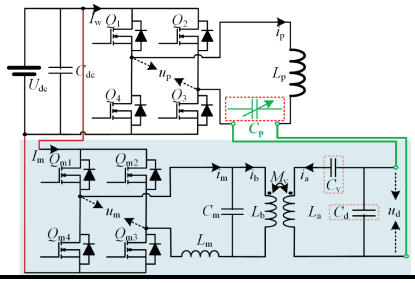	CMFC. **Number of circuit components:** Four MOSFETs, one inductor, one transformer, and three capacitors.	**The phase shift angle** of the CMFC's full-bridge inverter. By collecting i_p to synchronize the PWM signal.

used by the L filter. B_m is the peak magnetic flux density of the L filter. R_{Lm} and R_{Cm} are the resistances of the LC filter.

$$P_{trans} = \underbrace{I_a^2 R_a + I_b^2 R_b + V_a k f^c B_a^e + V_b k f^c B_b^e}_{\text{Transformer}} + \underbrace{I_m^2 R_{Lm} + V_m k f^c B_m^e + (I_m - I_b)^2 R_{Cm}}_{\text{LC filter}}. \quad \text{(A7)}$$

3) Power Loss Equation of the Full-Bridge Rectifier: In terms of the full-bridge rectifier, its power loss equation is given by (A8), where I_2 is the RMS value of the secondary side resonant current, V_{rf} is the diode's forward voltage, and r_{rd} is the diode's on resistance.

$$P_{Rectifier} = \frac{4\sqrt{2}}{\pi} V_{rf} I_2 + 2 r_{rd} I_2^2. \quad \text{(A8)}$$

C. Comparison Between the CMFC and Two Existing Similar Methods

Based on the literature research and previous research done by our laboratory on cases I and II in Table II, the WCSs with these two methods are optimized to their best performance. Then, the following benchmarks are used to ensure the fairness of the comparison to the greatest extent. When R_o is 8.33 Ω, corresponding to the maximum P_o, and no misalignment occurs, η of WCSs with the CMFC and cases I and II is designed to be the same. On this basis, the working performance of these three WCSs is compared to verify which is the best one to solve the article's proposed problem. The main parameters of these WCSs are listed in Table III. It further points out that different methods have their advantages. The comparison in this section is intended to illustrate several advantages of the CMFC, which suit this article's WCS for AGVs, over cases I and II. Besides, it is acknowledged that the CMFC has drawbacks in other aspects. For example, although MOSFETs in the CMFC suffer from lower current stress than those in SCC, the CMFC has a more complex circuit structure. In other words, in the process of designing a WCS, multiple compromises are usually needed, which is the basic principle that is generally adopted in the current research field of wireless charging.

TABLE III
MAIN PARAMETERS OF THE DESIGNED WCS WITH CMFC

Symbol	Value for case I	Value for case II
U_{bus}	200 V	200 V
f	80–90 kHz	85 kHz
L_p and L_s	227 μH and 36 μH	274 μH and 36 μH
C_{p1} and C_{p2}	N/A	20 nF and 30 nF
L_{b1} and C_{b1}	400 μH *and* 470 μF	N/A
M_{ps}	22.5 μH	25 μH
P_o	350 W	350 W
R_o	2.57–8.33 Ω	2.57–8.33 Ω

Note: Assuming that the magnetic coupler's receiver, which are stipulated in this article's project, remain the same, the coil turns of the transmitter, whose size remains unchanged, in cases I (N_T is 12) and II (N_T is 14) are optimized to realize the aforementioned comparison conditions.

1) Comparison Between the CMFC and Case I: Unlike the two-stage power adjustment circuit, which is a buck converter cascaded with a variable frequency controlled full-bridge inverter, the CMFC achieves the ZVS state and CP charging with one controllable variable, and further overcomes problems associated with case I, such as complex coordination control, relatively large system power loss, and secondary side resonant tank's detuning.

Fig. 22 further yields the following insights: In the absence of misalignment, η of the WCS with CMFC equals that of case I. However, as misalignment occurs, which corresponds to the decrease in L_p, the WCS with CMFC has a relatively higher η, especially when R_o is large. Meanwhile, when R_o is 2.57 Ω and misalignment occurs, the controllable range of the case I is much smaller than that of the CMFC. As indicated by the right coordinate axis, the power loss (P_{loss}) in the power regulation

circuit of case I is much greater than that of the CMFC. The power loss analysis validates the CMFC's advantages, given that the complexity of the power adjustment circuit is nearly identical between the CMFC and case I.

2) Comparison Between the CMFC and Case II: When juxtaposed with the SCC, although it features a simple structure, the CMFC's circuit component exhibits lower current or voltage stress, which further reduces the complexity and cost when selecting power devices, particularly when the WCS's system power level is high.

Although case II features a simple circuit, Fig. 23 yields the following conclusions: the maximum terminal voltage ($U_{\max}$) of MOSFETs in case II is larger than that of the CMFC, especially when Δx increases; although the CMFC's circuit structure is much more complex, η of the two compared methods are almost the same, because the CMFC usually ensures its regular operation by only using a small working current.

REFERENCES

[1] Y. Liu, Y. Li, J. Xu, S. Liu, J. Liu, and Z. He, "A constant current output method for low-voltage and high-current DWPT systems based on inverse coupled current doubler rectifier," *IEEE Trans. Power Electron.*, vol. 39, no. 8, pp. 9113–9119, Aug. 2024.

[2] X. Li, C. Wang, H. Wang, X. Dai, Y. Sun, and A. P. Hu, "A robust wireless power transfer system with self-alignment capability and controllable output current for automatic-guided vehicles," *IEEE Trans. Power Electron.*, vol. 38, no. 10, pp. 11898–11906, Oct. 2023.

[3] B. Yang et al., "Analysis and design of a T/S compensated IPT system for AGV maintaining stable output current versus air gap and load variations," *IEEE Trans. Power Electron.*, vol. 37, no. 5, pp. 6217–6228, May 2022.

[4] H. Zhang, Y. Chen, D. H. Kim, Z. Li, M. Zhang, and G. Li, "Variable inductor control for misalignment tolerance and constant current/voltage charging in inductive power transfer system," *IEEE J. Emerg. Sel. Topics Power Electron.*, vol. 11, no. 4, pp. 4563–4573, Aug. 2023.

[5] H. Wen et al., "A switchable dual-frequency LCC-S-S compensated three-coil WPT system for mobile desktop charging with constant current and constant voltage outputs," *IEEE Trans. Power Electron.*, vol. 40, no. 5, pp. 7586–7598, May 2025.

[6] R. Xie, Y. Wu, H. Tang, Y. Zhuang, and Y. Zhang, "A strongly coupled vehicle-to-vehicle wireless charging system for emergency charging purposes with constant-current and constant-voltage charging capabilities," *IEEE Trans. Power Electron.*, vol. 39, no. 4, pp. 3985–3989, Apr. 2024.

[7] R. Guo, C. Hu, and W. Shen, "An electric vehicle-oriented approach for battery multi-constraint state of power estimation under constant power operations," *IEEE Trans. Veh. Technol.*, vol. 73, no. 3, pp. 3300–3310, Mar. 2024.

[8] D. A. Z. Prada, A. El Aroudi, O. L. Santos, L. V. Seisdedos, and L. M. Salamero, "Constant power-constant voltage battery charging based on a loss-free resistor approach," *IEEE Trans. Circuits Syst. I, Reg. Papers*, vol. 71, no. 10, pp. 4778–4791, Oct. 2024.

[9] C. Ma, R. Yao, C. Li, and X. Qu, "A Family of IPT battery chargers with small clamp coil for configurable and self-sustained battery charging profile," *IEEE Trans. Power Electron.*, vol. 38, no. 6, pp. 7910–7919, Jun. 2023.

[10] K. Song et al., "Design of DD coil with high misalignment tolerance and low EMF emissions for wireless electric vehicle charging systems," *IEEE Trans. Power Electron.*, vol. 35, no. 9, pp. 9034–9045, Sep. 2020.

[11] J. Mai, Y. Wang, Y. Yao, M. Sun, and D. Xu, "High-misalignment-tolerant IPT systems with solenoid and double D pads," *IEEE Trans. Ind. Electron.*, vol. 69, no. 4, pp. 3527–3535, Apr. 2022.

[12] Y. Chen, R. Mai, Y. Zhang, M. Li, and Z. He, "Improving misalignment tolerance for IPT system using a third-coil," *IEEE Trans. Power Electron.*, vol. 34, no. 4, pp. 3009–3013, Apr. 2019.

[13] Z. Yuan, M. Saeedifard, C. Cai, Q. Yang, P. Zhang, and H. Lin, "A misalignment-tolerant design for a dual-coupled LCC-S-compensated WPT system with load-independent CC output," *IEEE Trans. Power Electron.*, vol. 37, no. 6, pp. 7480–7492, Jun. 2022.

[14] Y. Yao, Y. Wang, X. Liu, K. Lu, and D. Xu, "Analysis and design of an S/SP compensated IPT system to minimize output voltage fluctuation versus coupling coefficient and load variation," *IEEE Trans. Veh. Technol.*, vol. 67, no. 10, pp. 9262–9272, Oct. 2018.

[15] Y. Chen et al., "A hybrid inductive power transfer system with misalignment tolerance using quadruple-D quadrature pads," *IEEE Trans. Power Electron.*, vol. 35, no. 6, pp. 6039–6049, Jun. 2020.

[16] L. Zhao, D. J. Thrimawithana, and U. K. Madawala, "Hybrid bidirectional wireless EV charging system tolerant to pad misalignment," *IEEE Trans. Ind. Electron.*, vol. 64, no. 9, pp. 7079–7086, Sep. 2017.

[17] H. Feng, T. Cai, S. Duan, X. Zhang, H. Hu, and J. Niu, "A dual-side-detuned series–series compensated resonant converter for wide charging region in a wireless power transfer system," *IEEE Trans. Ind. Electron.*, vol. 65, no. 3, pp. 2177–2188, Mar. 2018.

[18] J. Yang, X. Zhang, K. Zhang, X. Cui, C. Jiao, and X. Yang, "Design of LCC-S compensation topology and optimization of misalignment tolerance for inductive power transfer," *IEEE Access*, vol. 8, pp. 191309–191318, 2020.

[19] C. Xia, W. Wang, S. Ren, X. Wu, and Y. Sun, "Robust control for inductively coupled power transfer systems with coil misalignment," *IEEE Trans. Power Electron.*, vol. 33, no. 9, pp. 8110–8122, Sep. 2018.

[20] J. M. Miller, O. C. Onar, and M. Chinthavali, "Primary-side power flow control of wireless power transfer for electric vehicle charging," *IEEE J. Emerg. Sel. Topics Power Electron.*, vol. 3, no. 1, pp. 147–162, Mar. 2015.

[21] Y. Jiang, J. Liu, X. Hu, L. Wang, Y. Wang, and G. Ning, "An optimized frequency and phase shift control strategy for constant current charging and zero voltage switching operation in series-series compensated wireless power transmission," in *Proc. IEEE Energy Convers. Congr. Expo.*, 2017, pp. 961–966.

[22] D. Patil, M. Sirico, L. Gu, and B. Fahimi, "Maximum efficiency tracking in wireless power transfer for battery charger: Phase shift and frequency control," in *Proc. IEEE Energy Convers. Congr. Expo.*, 2016, pp. 1–8.

[23] M. Pathmanathan, S. Nie, N. Yakop, and P. W. Lehn, "Field-oriented control of a three-phase wireless power transfer system transmitter," *IEEE Trans. Transp. Electrific.*, vol. 5, no. 4, pp. 1015–1026, Jul. 2019.

[24] A. Kamineni, G. A. Covic, and J. T. Boys, "Self-tuning power supply for inductive charging," *IEEE Trans. Power Electron.*, vol. 32, no. 5, pp. 3467–3479, Jul. 2017.

[25] K. Song et al., "A control strategy for wireless EV charging system to improve weak coupling output based on variable inductor and capacitor," *IEEE Trans. Power Electron.*, vol. 37, no. 10, pp. 12853–12864, Oct. 2022.

[26] W. Li, G. Wei, C. Cui, X. Zhang, and Q. Zhang, "A double-side self-tuning LCC/S system using a variable switched capacitor based on parameter recognition," *IEEE Trans. Ind. Electron.*, vol. 68, no. 4, pp. 3069–3078, Apr. 2021.

[27] Y. Li et al., "Extension of ZVS region of series–series WPT systems by an auxiliary variable inductor for improving efficiency," *IEEE Trans. Power Electron.*, vol. 36, no. 7, pp. 7513–7525, Jul. 2021.

[28] Y. Yang, J. Zeng, and S. Y. R. Hui, "A fast primary-side current and voltage control for direct wireless battery chargers," *IEEE J. Emerg. Sel. Topics Power Electron.*, vol. 12, no. 1, pp. 355–366, Feb. 2024.

[29] T. S. Chan and C. L. Chen, "A primary side control method for wireless energy transmission system," *IEEE Trans. Circuits Syst. I, Reg. Papers*, vol. 59, no. 8, pp. 1805–1814, Aug. 2012.

[30] L. Yang, X. Li, S. Liu, Z. Xu, C. Cai, and P. Guo, "Analysis and design of three-coil structure WPT system with constant output current and voltage for battery charging applications," *IEEE Access*, vol. 7, pp. 87334–87344, 2019.

[31] Y. Jiang, L. Wang, J. Fang, R. Li, R. Han, and Y. Wang, "A high-efficiency ZVS wireless power transfer system for electric vehicle charging with variable angle phase shift control," *IEEE J. Emerg. Sel. Topics Power Electron.*, vol. 9, no. 2, pp. 2356–2372, Apr. 2021.

[32] L. Colak, E. Asa, M. Bojarski, D. Czarkowski, and O. C. Onar, "A novel phase-shift control of semibridgeless active rectifier for wireless power transfer," *IEEE Trans. Power Electron.*, vol. 30, no. 11, pp. 6288–6297, Nov. 2015.

[33] J. Li, L. Zhang, X. Wu, Z. Zhou, and Q. Chen, "Adaptive tube-based model predictive control for the receiving-side DC–DC of dynamic wireless power transfer system," *IEEE J. Emerg. Sel. Topics Power Electron.*, vol. 12, no. 5, pp. 5323–5336, Oct. 2024.

[34] Z. Huang, C. S. Lam, P. I. Mak, R. P. S. Martins, S. C. Wong, and C. K. Tse, "A single-stage inductive-power-transfer converter for constant-power and maximum-efficiency battery charging," *IEEE Trans. Power Electron.*, vol. 35, no. 9, pp. 8973–8984, Sep. 2020.

[35] F. Xu, S. C. Wong, and C. K. Tse, "Overall loss compensation and optimization control in single-stage inductive power transfer converter delivering constant power," *IEEE Trans. Power Electron.*, vol. 37, no. 1, pp. 1146–1158, Jan. 2022.
[36] X. Li, B. Sun, J. Xu, S. Pang, and H. Li, "Design and analysis of misalignment insensitive wireless power transfer system based on multitransmitter for constant power," *IEEE J. Emerg. Sel. Topics Power Electron.*, vol. 11, no. 4, pp. 4536–4548, Aug. 2023.
[37] Z. Luo, Y. Zhao, M. Xiong, X. Wei, and H. Dai, "A self-tuning LCC/LCC system based on switch-controlled capacitors for constant-power wireless electric vehicle charging," *IEEE Trans. Ind. Electron.*, vol. 70, no. 1, pp. 709–720, Jan. 2023.
[38] X. Zhang, R. Xue, F. Wang, F. Xu, T. Chen, and Z. Chen, "Capacitor tuning of LCC-LCC compensated IPT system with constant-power output and large misalignments tolerance for electric vehicles," *IEEE Trans. Power Electron.*, vol. 38, no. 10, pp. 11928–11939, Oct. 2023.
[39] Y. Gu, J. Wang, Z. Liang, and Z. Zhang, "Flexible constant-power range extension of self-oscillating system for wireless in-flight charging of drones," *IEEE Trans. Power Electron.*, vol. 39, no. 11, pp. 15342–15355, Nov. 2024.
[40] Y. Zhang, K. Chen, F. He, Z. Zhao, T. Lu, and L. Yuan, "Closed-form oriented modeling and analysis of wireless power transfer system with constant-voltage source and load," *IEEE Trans. Power Electron.*, vol. 31, no. 5, pp. 3472–3481, May 2016.
[41] Z. Luo, Y. Zhao, M. Xiong, X. Wei, and H. Dai, "A self-tuning LCC/LCC system based on switch-controlled capacitors for constant-power wireless electric vehicle charging," *IEEE Trans. Ind. Electron.*, vol. 70, no. 1, pp. 709–720, Jan. 2023.
[42] Z. Huang, C.-S. Lam, P.-I. Mak, R. P. d S. Martins, S.-C. Wong, and C. K. Tse, "A single-stage inductive-power-transfer converter for constant-power and maximum-efficiency battery charging," *IEEE Trans. Power Electron.*, vol. 35, no. 9, pp. 8973–8984, Jan. 2020.
[43] X. Zhang, R. Xue, F. Wang, T. Chen, and Z. Chen, "Capacitor tuning of LCC-LCC compensated IPT system with constant-power output and large misalignments tolerance for electric vehicles," *IEEE Trans. Power Electron.*, vol. 38, no. 10, pp. 11928–11939, Oct. 2023.
[44] Y. Chen, B. Yang, Z. Kou, Z. He, G. Cao, and R. Mai, "Hybrid and reconfigurable IPT systems with high-misalignment tolerance for constant-current and constant-voltage battery charging," *IEEE Trans. Power Electron.*, vol. 33, no. 10, pp. 8259–8269, Oct. 2018.
[45] Y. Zhang, Y. Zhou, Y. Zheng, R. Xie, X. Chen, and X. Mao, "Dual-channel wireless power transfer systems with reconfigurable series-parallel switchers on both input and output ports for wide constant-voltage or constant-current range and misalignment tolerance," *IEEE Trans. Ind Electron.*, vol. 72, no. 8, pp. 7974–7982, Aug. 2025.
[46] K. Song et al., "An impedance decoupling-based tuning scheme for wireless power transfer system under dual-side capacitance drift," *IEEE Trans. Power Electron.*, vol. 36, no. 7, pp. 7526–7536, Jul. 2021.
[47] B. X. Nguyen et al., "An efficiency optimization scheme for bidirectional inductive power transfer systems," *IEEE Trans. Power Electron.*, vol. 30, no. 11, pp. 6310–6319, Nov. 2015.
[48] H. Hu, T. Cai, S. Duan, X. Zhang, J. Niu, and H. Feng, "An optimal variable frequency phase shift control strategy for ZVS operation within wide power range in IPT systems," *IEEE Trans. Power Electron.*, vol. 35, no. 5, pp. 5517–5530, May 2020.

Zhenjie Li (Member, IEEE) received the B.S. degree in measurement and control technology and instrumentation from the School of Measurement and Control Technology and Communication Engineering, Harbin University of Science and Technology, Harbin, China, in 2012, and the M.S. degree in instrument science and technology and Ph.D. degree in electric engineering from the School of Electrical Engineering and Automation, Harbin Institute of Technology, Harbin, China, in 2014 and 2020, respectively.

Since 2020, he has been an Associate Professor with the College of Computer and Control Engineering, Northeast Forestry University, Harbin, China. He authored or coauthored a highly cited ESI paper in the IEEE TRANSACTIONS ON POWER ELECTRONICS. His research interests include designing and controlling the wireless charging system with multiple applications and power levels.

Prof. Li was the recipient of the 2023 and 2024 Star Reviewer Award from the IEEE JOURNAL OF EMERGING AND SELECTED TOPICS IN POWER ELECTRONICS.

Qihao Dong received the B.S. degree in electric engineering from the College of Information and Control Engineering, Liaoning Petrochemical University, Fushun, China, in 2021. He is currently working toward the master's degree in control science and engineering from Northeast Forestry University, Harbin, China.

His research interests include lightweight design and optimization of wireless power transfer systems.

Yuhong Bai received the B.S. degree in electric engineering from the School of Management and Engineering, Nanjing University, Nanjing, China, in 2020. He is currently working toward the Ph.D. degree in mechanical engineering with Northeast Forestry University, Harbin, China.

His research interests include modeling, multiple parameter optimization, parameter identification, and magnetic coupling structure design.

Dechun Yuan received the B.S. degree in communication engineering and the M.S. and Ph.D. degrees in automation of forest engineering from Northeast Forestry University, Harbin, China, in 2007, 2011, and 2017, respectively.

He is currently with the College of Computer and Control Engineering, Northeast Forestry University. His current research focuses on multiscenario wireless charging technology.

Yiqi Liu (Member, IEEE) received the B.S. degree in electrical engineering from the Northeast Agriculture University, Harbin, China, in 2009, the M.S. degree in electrical engineering from the Tianjin University of Technology, Tianjin, China, in 2012, and the Ph.D. degree in electrical engineering from the Harbin Institute of Technology, Harbin, China, in 2016.

From 2013 to 2015, he was a visiting Ph.D. student with the Center for Ultra-Wide-Area Resilient Electric Energy Transmission Networks, University of Tennessee, Knoxville, TN, USA, with support from CSC. In 2016, he joined Northeast Forestry University as an Associate Professor. Since 2022, he has been a Professor. His research interests include power electronics for renewable energy sources, multilevel converters, high-voltage direct-current technology, dc microgrids, energy conversion, and wireless power transfer systems.